



Article

# Corrosion Behavior of AZ31B Magnesium Alloy Anode by Sulfate-Reducing Prokaryotes in the Tidal Flat Mud with Different Water Contents

Jinrong Li <sup>1,2,3,4</sup>, Ruiyong Zhang <sup>2,4,\*</sup> , Wolfgang Sand <sup>5,6</sup> , Qingjun Zhu <sup>2,4</sup> , Xin Liu <sup>1,\*</sup>, Jizhou Duan <sup>2,4</sup> , Baorong Hou <sup>2,4</sup> and Jie Zhang <sup>2,3,4,\*</sup>

<sup>1</sup> College of Materials Science and Engineering, Qingdao University of Science and Technology, Qingdao 266042, China

<sup>2</sup> Key Laboratory of Marine Environmental Corrosion and Bio-Fouling, Institute of Oceanology, Chinese Academy of Sciences, Qingdao 266071, China

<sup>3</sup> Institute of Marine Corrosion Protection, Guangxi Academy of Sciences, Nanning 530007, China

<sup>4</sup> Open Studio for Marine Corrosion and Protection, Pilot National Laboratory for Marine Science and Technology (Qingdao), Qingdao 266237, China

<sup>5</sup> Institute of Biosciences, University of Mining and Technology, 09599 Freiberg, Germany

<sup>6</sup> Department of Aquatic Biotechnology, Faculty of Chemistry, University of Duisburg-Essen, 45141 Essen, Germany

\* Correspondence: ruiyong.zhang@qdio.ac.cn (R.Z.); liuxin@qust.edu.cn (X.L.); zhangjie@qdio.ac.cn (J.Z.); Tel.: +86-532-82898851 (R.Z. & J.Z.); +86-18366235518 (X.L.)

**Abstract:** At present, there are few studies on microbial corrosion of magnesium anode materials that provide protection for oil pipelines in tidal flat environment. In view of an abnormal failure of magnesium anodes in oil pipelines in a tidal flat mud environment, the influence of the change in water content in the beach mud on the corrosion of AZ31B magnesium anode by sulfate-reducing prokaryote (SRP) was investigated by electrochemical methods, weight loss and surface analysis techniques. SRP can grow well in a tidal flat mud environment and cause microbial corrosion of magnesium alloy. The results show that with the increase in water content, the number of SRP cells in the mud increased, that the corrosivity of tidal flat muds was enhanced and that the corrosion rate of AZ31B magnesium anode was accelerated: compared with the corrosion rate of 0.554 mm/y in 40% water content, the corrosion rate of magnesium alloy samples in 60% water content is as high as 1.38 mm/y.

**Keywords:** sulfate-reducing prokaryotes; water content; AZ31B magnesium anode; tidal flat soil



**Citation:** Li, J.; Zhang, R.; Sand, W.; Zhu, Q.; Liu, X.; Duan, J.; Hou, B.; Zhang, J. Corrosion Behavior of AZ31B Magnesium Alloy Anode by Sulfate-Reducing Prokaryotes in the Tidal Flat Mud with Different Water Contents. *Lubricants* **2022**, *10*, 293.

<https://doi.org/10.3390/lubricants10110293>

Received: 24 September 2022

Accepted: 30 October 2022

Published: 2 November 2022

**Publisher's Note:** MDPI stays neutral with regard to jurisdictional claims in published maps and institutional affiliations.



**Copyright:** © 2022 by the authors. Licensee MDPI, Basel, Switzerland. This article is an open access article distributed under the terms and conditions of the Creative Commons Attribution (CC BY) license (<https://creativecommons.org/licenses/by/4.0/>).

## 1. Introduction

Magnesium alloys have been experiencing a steady increase in interest in demand due to many advantages, such as high specific strength, low density [1], high thermal conductivity, good electromagnetic properties [2], excellent casting and recycling ability [3]. At the same time, sacrificial anode materials made of a magnesium alloy have a high electrochemical performance and high energy yield per mass unit. It is suitable for cathodic protection of metal structures in high-resistivity media, such as soil and fresh water [4]. Regarding the research on corrosion protection of metal pipelines, corrosion problems, such as uniform corrosion, pitting corrosion, stray current corrosion and microbial-influenced corrosion (MIC), in pipelines have been widely studied [5,6]. Different from the corrosion research of pipeline steel, most of the corrosion research on magnesium alloy materials focuses on the corrosion of different alloys in different solutions [7], atmospheric corrosion [8] and anti-corrosion coating [9]. However, little attention has been paid to the corrosion of magnesium anodes used to protect pipes. Due to their inherent low corrosion resistance [10], magnesium anodes often fail abnormally due to unstable discharge before

reaching the expected service life. In the cathodic protection of buried pipelines in a tidal flat environment, whether magnesium anode can provide stable protective current for a pipeline is also closely related to pipeline safety.

The corrosion behavior of magnesium alloys under various conditions has been studied widely [11,12]. There are many factors influencing the corrosion rate and mechanism of magnesium alloys, such as the pH value [13], addition of different alloying elements in magnesium [14], different kinds of ions and different concentrations of ions [15,16], which have a significant impact on the corrosion resistance of magnesium alloys. Pipeline corrosion, which is widely studied by researchers, is influenced by a large number of factors, such as soil resistivity, soil chemistry, pH and microorganisms [17]. Microbial corrosion is considered as one of the most aggressive factors in nature [18] and one of the main factors causing pipeline failure [19,20]. Sulfate-reducing prokaryotes (SRPs) are one of the most prone anaerobic microorganisms to cause microbiologically influenced corrosion (MIC), whose activity results in more than 50% of all microbial corrosion cases in natural environments [21,22]. The corrosion of pipelines caused by SRP receives considerable attention [23]. However, the research on SRP causing corrosion of magnesium anodes has been ignored largely. Different researchers have reached different conclusions in their studies: it is found that magnesium alloy material surface can form biofilm in the surface of a medium containing SRP and the presence of the biofilm significantly reduces the corrosion sensitivity of magnesium alloy to  $\text{Cl}^-$  [24]. At the same time, SRP can accelerate the micro-galvanic corrosion of magnesium alloy surface by cathode depolarization [25].

With the development of the offshore oil industry, more and more oil and gas pipelines are constructed in the sea. The metal pipelines are located in different environments, such as sea mud, sea water and beach. Subsequently, magnesium alloy anode materials, which provide protection for these pipelines, are exposed to a variety of environmental conditions. The tidal flat environment, as a kind of wetland, has unique ecological characteristics. However, most previous studies focused on the corrosivity of seabed sediments [26,27]. There are only a few reports on metal corrosion in tidal flat environments. In fact, from the perspective of water content, salt content and air permeability, the tidal flat environment is largely different from common mud and marine sediments. These factors may significantly change the activity of SRP in the sea mud environment and affect the corrosion process of magnesium anodes.

Up to now, there are limited studies on the corrosion of magnesium alloys by SRP in the environment of tidal flat mud. In this work, the mud samples obtained from the actual tidal flat environment were analyzed. The experimental system was designed with reference to the water content parameters in this environment. By means of weightless tests, surface analysis and electrochemical tests, the corrosion by tidal flat mud was studied. The microbial corrosion mechanism of the AZ31B magnesium alloy sacrificial anode material by SRP under different water content conditions was explored and discussed.

## 2. Materials and Methods

### 2.1. Materials

The coupons of the AZ31B magnesium anodes were provided by Zibo Deyuan Metal Materials Co., Ltd. (Shandong, China). The composition is shown in Table 1. The processed  $10\text{ mm} \times 10\text{ mm} \times 4\text{ mm}$  cuboids were used to prepare the working electrodes for electrochemical testing. Degreasing was carried out by ultrasound for 5 min with acetone and absolute ethanol, respectively. Then the coupons were dried under a high-purity  $\text{N}_2$  atmosphere. A surface area of  $10\text{ mm} \times 10\text{ mm}$  was exposed to the solution, whereas the rest was sealed with epoxy resin. Before the test, surfaces were polished with silicon carbide sandpaper with 800, 1000, 1500, 2000 and 3000 particle size step by step. A  $20\text{ mm} \times 50\text{ mm} \times 4\text{ mm}$  sample was used for the weightless determination. An ultraviolet (UV) lamp was used to disinfect all samples for 30 min prior to testing [28].

**Table 1.** Chemical composition (in wt.%) of AZ31B.

Mg	Alloying Elements			Fe	Impurity Elements ( $\leq$ )			
	Al	Zn	Mn		Cu	Ni	Si	Ca
Bal	2.5~3.5	0.60~1.40	0.20~1.0	0.003	0.01	0.001	0.08	0.04

## 2.2. Tidal Flat Mud Conditions

The mud samples were taken from the tidal flat area, where the pipeline had been laid at the first station of Hengqin on the west coast of Dahengqin Island in Zhuhai, Guangdong Province, China. After drying and grinding, the tidal flat mud was sieved ( $\phi 800$ ) and autoclaved at 120 °C for 20 min before the experiment started. Then, 4 mL of bacterial solution with an initial cell concentration of approximately  $1 \times 10^6$  cells/mL was added to 100 mL of Postgate C (PGC) medium in an anaerobic incubator. The medium was then mixed with the dried and sterilized mud in different proportions to achieve different water contents. The names of chemicals and reagents used for PGC medium are shown in Table 2.

**Table 2.** Composition of Postgate C (PGC) medium.

KH <sub>2</sub> PO <sub>4</sub>	0.25 g
NH <sub>4</sub> Cl	0.5 g
CaCl <sub>2</sub> ·6H <sub>2</sub> O	0.03 g
MgSO <sub>4</sub> ·7H <sub>2</sub> O	0.06 g
70% sodium lactate	3 mL
Yeast Extract	0.5 g
Na <sub>3</sub> C <sub>6</sub> H <sub>5</sub> O <sub>7</sub> (trisodium citrate)	0.15 g
aged seawater	500 mL

pH = 7.2 ± 0.2.

## 2.3. Bacterium and Culture Media

The SRP strain used in this work was *Desulfovibrio* sp. HQM3. It was isolated from the tidal flat sediments near the pipeline on the west coast of Dahengqin Island (113.45° E, 22.12° N), Zhuhai City, Guangdong Province [29]. Microbial cells were cultured using Postgate C (PGC) medium. All solutions were deoxygenated using filtered N<sub>2</sub> for 30 min. Anaerobic vials and solutions were autoclaved at 120 °C for 20 min. The inoculated SRPs were incubated at 30 °C for 3–5 days.

## 2.4. Weight-Loss Determination

AZ31B magnesium anode test pieces with dimensions of 20 mm × 50 mm × 4 mm was used for the weight-loss determination. After weighing, the samples were buried in mud containing SRPs for a period of 14 d. Three parallels were conducted. A dedusting solution (CrO<sub>2</sub> 150 g/L and Ag<sub>2</sub>CrO<sub>4</sub> 10 g/L) was used to remove adhering corrosion products. The whole operation was carried out under anaerobic conditions. The samples were re-weighed according to the national standard (GB/T39637-2020). The calculation for the corrosion rate is as follows:

$$v = 8.76 \times \frac{w_0 - w_1}{AT\rho}$$

$v$  is the average corrosion rate of the sample (mm/a),  $w_0 - w_1$  is the weight of the removed of corrosion products (g),  $A$  is the sample area (m<sup>2</sup>),  $T$  is the test duration of the cycle (h) and  $\rho$  is the density of magnesium anode (1.78 g/cm<sup>3</sup>).

## 2.5. Surface Characterization

After removing corrosion products, the depth of the corrosion pits was measured by confocal laser scanning microscopy (CLSM, LEXT OLS5000, Olympus, Tokyo, Japan). Scanning electron microscopy (SEM, JEOL-7610F, Tokyo, Japan) was used to observe the

morphology of the corrosion products, the biofilm and the surface morphology after corrosion. For SEM observation, the coupons were immersed in 2.5% (*v/v*) glutaraldehyde solution for 3–5 h and then serially dehydrated in ethanol solutions (30%, 50%, 70%, 90% and 100%). Afterwards, the dehydrated samples were dried by supercritical CO<sub>2</sub> [30]. Before observation, a thin gold film with a thickness of 0.5 μm was sputtered on the sample surface to improve the electrical conductivity.

X-ray diffractometer (XRD) (Rigaku D/ MAX-3C, Tokyo, Japan) was used to determine the composition of the corrosion products. The XRD patterns were collected from 5° to 80° at a rate of 10°/min.

## 2.6. Electrochemical Corrosion Tests

The electrochemical tests were measured using a Gamry 3000 Electrochemical Analyzer (Warminster, PA, USA). The AZ31B magnesium anode samples were embedded in epoxy resin and were used as working electrode (WE). A saturated calomel electrode (SCE) and a platinum plate electrode were used as reference electrode (RE) and counter electrode (CE). Electrochemical impedance spectroscopy (EIS) was performed at the open circuit potential (OCP) in a frequency range of 10<sup>-2</sup> to 10<sup>5</sup> Hz with a 10 mV amplitude sinusoidal alternating current voltage signal. A Tafel polarization curve was conducted at a sweep rate of 0.167 mV/s. ZsimpWin Version 3.60 was used for curve fitting of the data. The linear polarization-resistance (LPR) scan ranges were recorded from −1 mV to 1 mV and were compared to the stable open circuit potential. All measurements were made at 25 ± 2 °C. Three groups of parallel samples were set up for each experiment.

## 3. Results

### 3.1. Cell Count

At the end of the 14-day experiment, the attached bacteria on the test sheets were counted using the most probable number (MPN) counting method according to the national standard GB/T14643. Table 3 shows the counts of SRP cells attached to the samples after 14 d of testing under different water contents. Three water contents for the tidal flat mud were selected, namely, the mass ratio of mud to water (actually a mixed solution of seawater medium containing 4% SRP concentration) was 6:4, 5:5 and 4:6. The simulated mud water content in this work refers to the actual water content measured for the actual buried pipeline [29]. The number of sessile SRP cells increased significantly with the increase in the water content. This indicates that moisture is an important parameter for SRP growth in the tidal flat mud. The SRP growth is better in the mud with increased water content, as expected.

**Table 3.** Counts of SRP cells (sessile) attached to AZ31B magnesium anodes initially and after 14 d of testing with varied water contents. Water content is the mass fraction of sea water in mud.

Water Content	Sessile SRP Count (Cells/cm <sup>2</sup> )
40%	(2.40 ± 0.01) × 10 <sup>4</sup>
50%	(5.50 ± 0.01) × 10 <sup>4</sup>
60%	(8.05 ± 0.01) × 10 <sup>4</sup>

### 3.2. Surface Characterization

Figure 1 shows selected SEM images of the surface films formed on the samples after 14 d in muds at different humidity. In general, a dense surface film can effectively prevent the corrosion process of the metal matrix [31,32]. In the presence of SRP, the surface films were composed of biofilms and corrosion products. The corrosion products on the surface appeared loose and dispersed (Figure 1b). The surface film that formed at a low water content of 40% (Figure 1a) was mainly composed of corrosion products, while SRPs were detected seldomly. Cracks and pores can be observed in the corrosion product film (Figure 1b). As the water content was increased to 60%, the surface film became slightly

dense, containing corrosion products and obvious SRP cells (Figure 1c). Nevertheless, the corrosion products had a granular distribution and existed in layers. Further, large corrosion product particles could be observed. SRP cells were observed between layers. These results showed that SRPs can grow well in a tideland environment. The corrosion product film that formed on the surface appeared loose and porous, which probably cannot effectively hinder the corrosion progress.

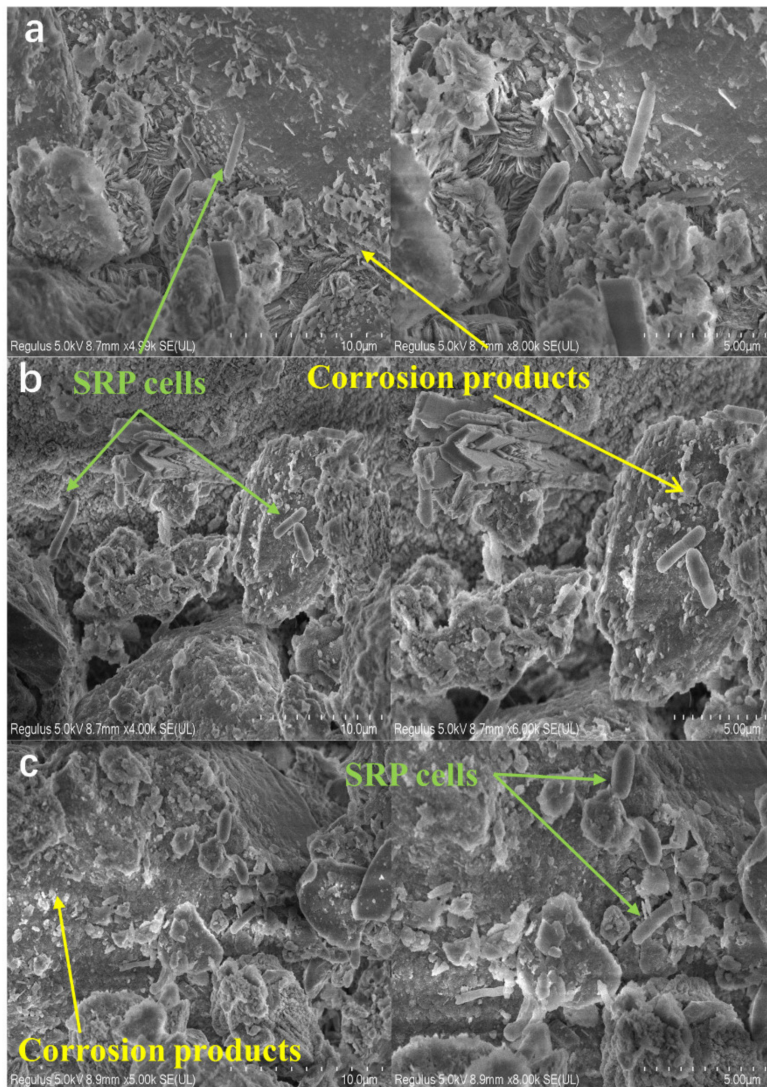


**Figure 1.** Selected SEM images of surface films formed on AZ31B magnesium alloy specimen after 14 days of testing in the tidal flat mud with varied conditions: (a): tidal flat mud with water content 40%; (b): tidal flat mud with water content 50%; (c): tidal flat mud with water content 60%.

The XRD results are shown in Figure 2. The main corrosion product was  $3\text{MgO}\cdot2\text{SiO}_2\cdot2\text{H}_2\text{O}$ . Since the sample was immersed in tidal flat mud, the presence of some soil residues ( $\text{SiO}_2$ ) is not surprising, as these may have not been removed completely. Sulfide produced by the sulfate reduction of SRPs was not detected. This may be due to the fact that  $\text{Mg}^{2+}$  would undergo a double-hydrolysis reaction with  $\text{S}^{2-}$ . The Mg matrix peak was not detected in the XRD pattern. This result indicates that the surface of the AZ31B magnesium alloy was covered by a corrosion product layer and biofilms. The magnesium anode matrix was not exposed.

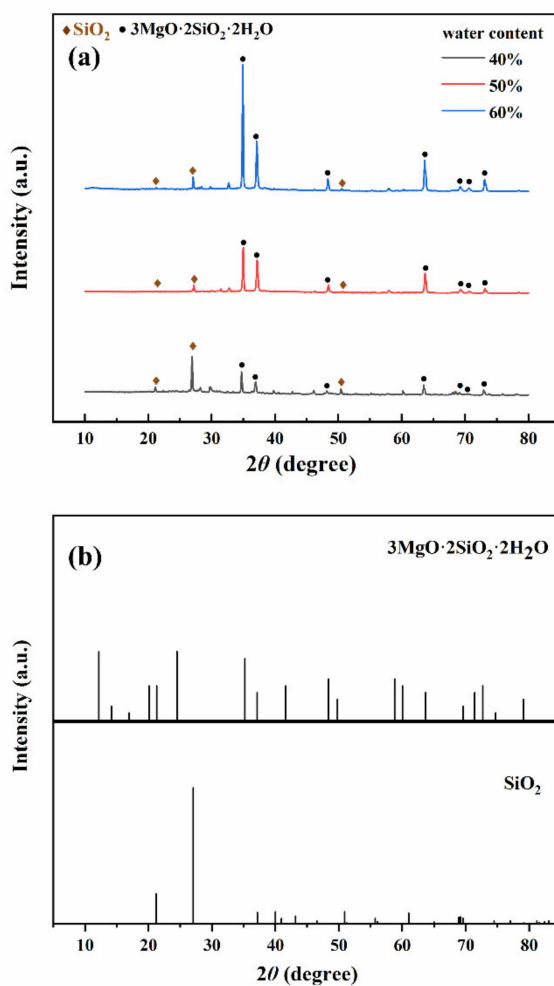
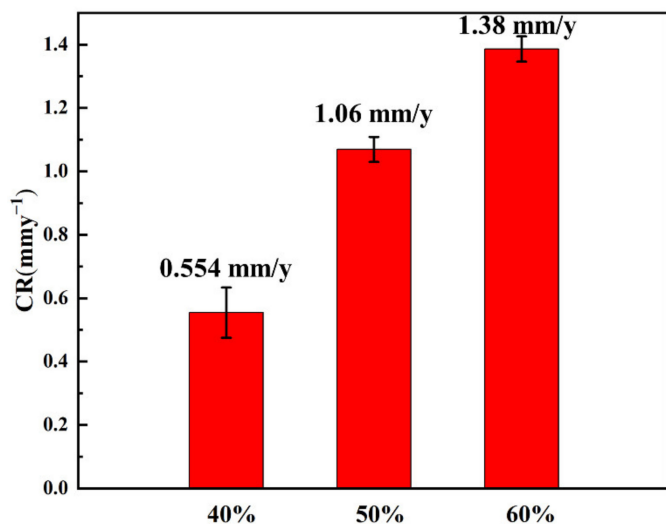


**Figure 2.** Selected XRD patterns of the surface films formed on the AZ31B magnesium alloy specimen after 14 days of immersion in tidal flat mud at different water contents (a): 40%, 50% and 60% and corresponding standard peaks (b).

Figure 2 shows that the composition of the corrosion products under different water contents was similar. However, the XRD peak intensities of the products from different assays are different. The peak intensity of the XRD pattern can reflect the crystallinity and thickness of the corrosion product film [33]. For the samples with high water content, an increased peak value for the corrosion products appeared, if compared with those under low water content. Thus, the samples were subjected to more serious corrosion and produced a thicker corrosion product layer for tests with high water content than for those with low water content.

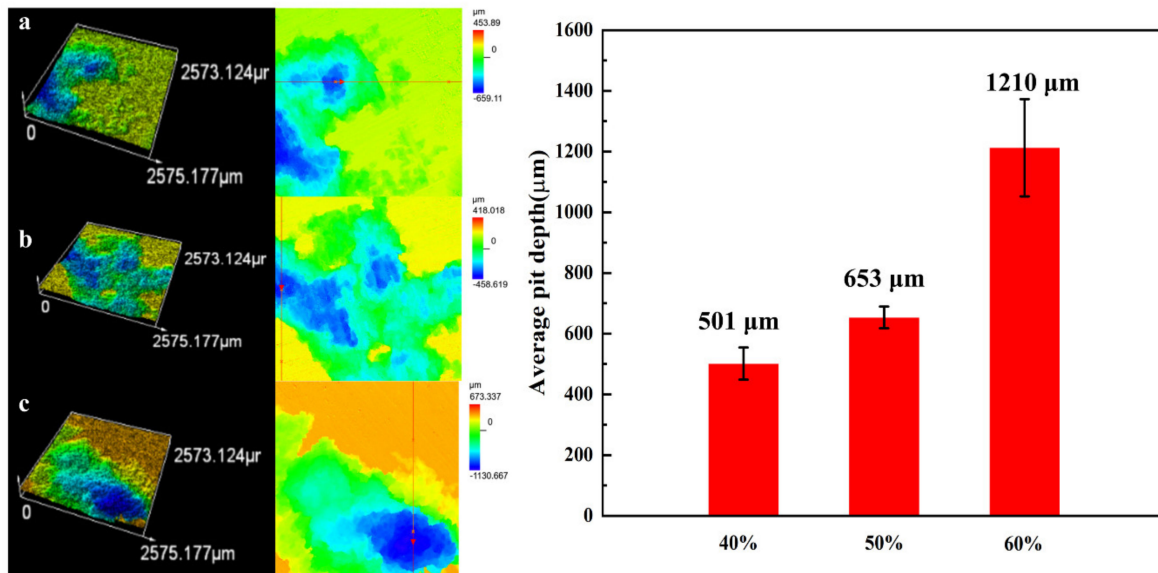
### 3.3. Weightless and Pitting Corrosion

Figure 3 shows the corrosion rate of the AZ31B magnesium alloy anode material, calculated from weight-loss measurements after 14 d. The corrosion rate increased with the increase in mud water content. If the mud water content was 40%, 50% or 60%, the corrosion rate amounted to 0.554 mm/y, 1.06 mm/y or 1.38 mm/y, respectively. The corrosion rate of AZ31B magnesium anode in the assays with 60% moisture content was 2.5-times higher than those with 40% moisture content. This indicates that the increase in the water content in mud enhanced the corrosion of the AZ31B magnesium anode by SRP.



**Figure 3.** Corrosion rates for AZ31B magnesium anodes from weight-loss measurements after 14 days of testing in tidal flat mud under varied conditions of water content. The ratios marked in the x-axis are the seawater content.

The pitting depth was measured on the surface of the AZ31B magnesium anode sample. As shown in Figure 4, if the mud water content was 40%, 50% or 60%, the average pitting pit depth measured was 0.501 mm, 0.653 mm and 1.21 mm, respectively. The average pitting depth for the AZ31B magnesium anode in 60% water content mud was 2.4-times higher than that with 40% water content. The trend of the average pit depth was consistent with the weight loss.



**Figure 4.** CLSM images of the AZ31B magnesium alloy coupons after 14 days of testing in tidal flat mud under varied conditions (after removal of the surface products): (a): tidal flat mud with seawater content 40%; (b): tidal flat mud with seawater content 50%; (c): tidal flat mud with seawater content 60%. The ratios marked in the x-axis are the seawater content.

### 3.4. Electrochemical Analysis

Figure 5 shows the open-circuit potential diagrams measured during the experiment. To some extent, the open-circuit potential diagrams reflect the thermodynamic tendency of metal corrosion. A negative open-circuit potential indicates an increased tendency for metal corrosion [34]. As can be seen in Figure 5, the open-circuit potential shows

an increasing trend in the first 1–3 d. The formation of biofilms can generally promote the forward development of the OCP [35,36]. Biofilms, formed in the early stage of the experiment, can hinder corrosion to some extent. The results from the subsequent 5–13 d of experiment show that the higher the water content, the lower the OCP of the sample and the higher the corrosion tendency.

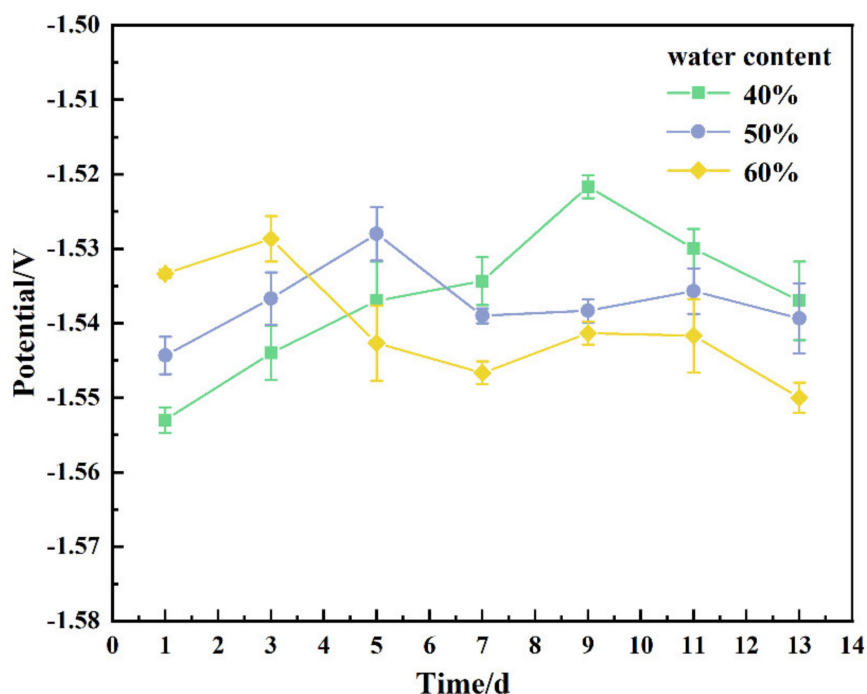


**Figure 5.** OCP values for the AZ31B magnesium alloy coupons after 14 days of testing in tidal flat mud under varied conditions of seawater content (40%, 50% or 60%, respectively).

The EIS measurements were carried out with tidal flat mud and different water contents. The Nyquist and Bode diagrams are shown in Figure 6. The data were analyzed using ZsimpWin version 3.50. The mean variance  $\chi^2$  of the measured and fitted data was used to determine the fitting quality of the equivalent circuit in order to ensure that it amounted to less than  $10^{-3}$  [37]. The results show that the diameter of the capacitive arc in the Nyquist diagram is proportional to the corrosion resistance of the electrode samples [38]. Data in Figure 6 show that at the early stage of the experiment (1–3 d), the low-frequency region and high-frequency region in the Nyquist plot were composed of a capacitor arc, which corresponded to the occurrence of uniform corrosion on the sample. From the fifth day onwards, the capacitor arc in the low-frequency region disappeared and the inductor arc appeared, which indicates the beginning of pitting corrosion [39]. The radius of the capacitor arc in the high-frequency region decreased first and then increased over time, which indicates that the corrosion rate of the sample increased first and then decreased. With the progress of corrosion, the corrosion product layer on the surface increased in thickness, which led to an increased difficulty for charge transfer and, consequently, slowed down the corrosion rate.

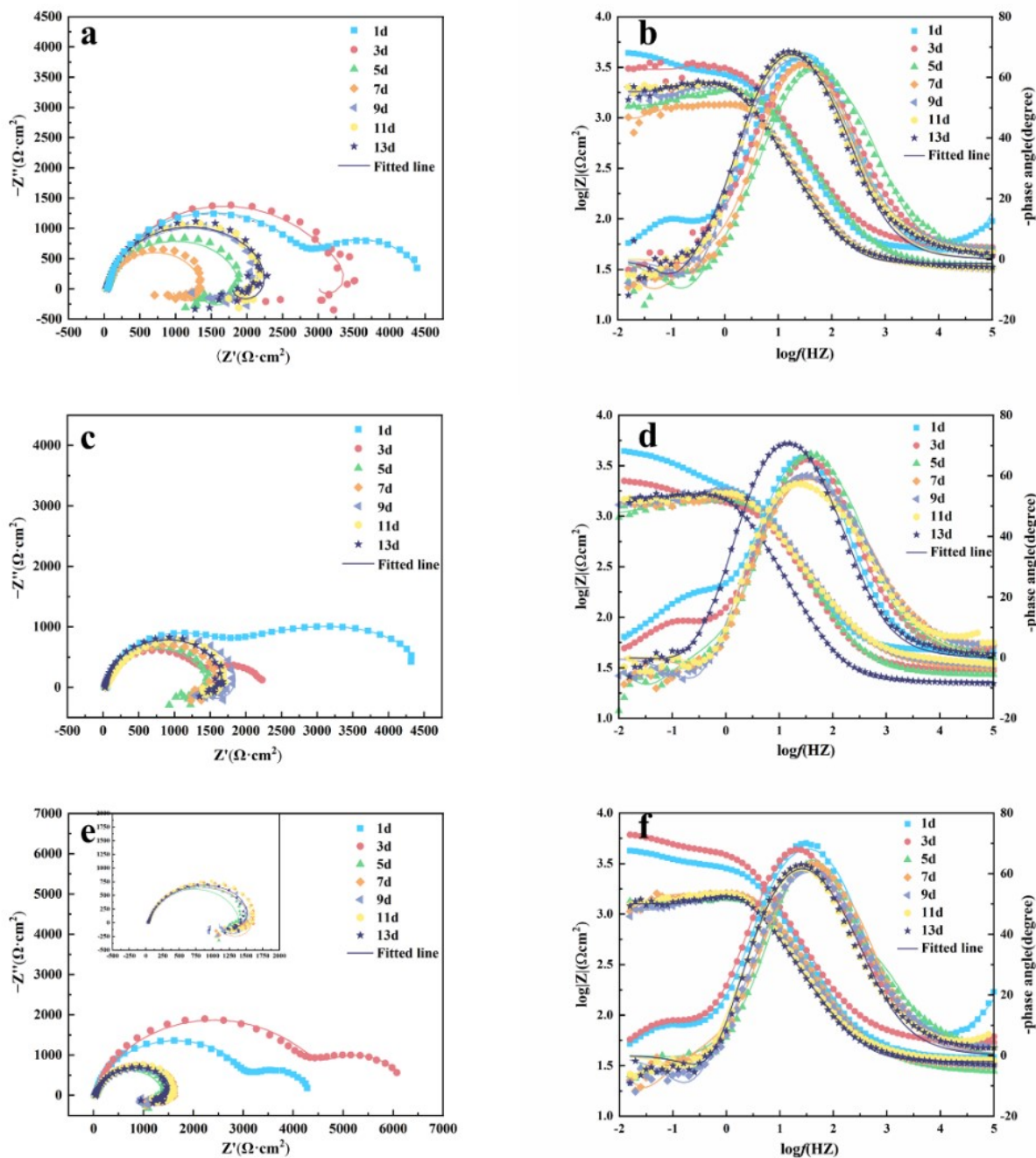


**Figure 6.** Nyquist diagrams and Bode plots for the AZ31B magnesium anode during the 13 days testing time with a tidal flat mud under varied conditions: (a,b): tidal flat mud with seawater content 40%; (c,d): tidal flat mud with seawater content 50%; (e,f): tidal flat mud with seawater content 60%.

The equivalent circuit diagram in Figure 7 is used to fit the impedance data, from which the fitting parameters of the circuit elements in Tables 4–6 is obtained.  $R_{\text{sol}}$  stands for solution resistance;  $Q_f$  and  $R_f$  represent the capacitance and resistance of corrosion product film and biofilm, respectively.  $Q_{\text{dl}}$  and  $R_{\text{ct}}$  correspond to double-layer capacitance and charge transfer resistance, respectively. Due to the inhomogeneity of the specimen surface caused by corrosion, the impedance data were fitted using the constant phase Angle element ( $Q$ ) instead of the standard capacitance ( $C$ ). The impedance of  $Q$  can be calculated by the following formula [40]:

$$Z_{\text{CPE}} = Y_0^{-1}(jw)^{-n}$$

in which  $w$  is the angular frequency (rad/s) and  $Y_0$  and  $n$  are the exponents, indicating that the sample deviates from the ideal capacitance [41]. The inductance in the low-frequency region is expressed by  $L_{\text{pit}}$ . The generation of low-frequency inductance is generally attributed to the adsorption and the peeling of reactants on the surface of the metal matrix and the pitting behavior.  $n$  is the dispersion coefficient ( $0 < n < 1$ ), which represents the deviation from the ideal capacitance. A value for  $n = 1$  represents a perfect capacitor, whereas 0 represents a perfect resistance [42].

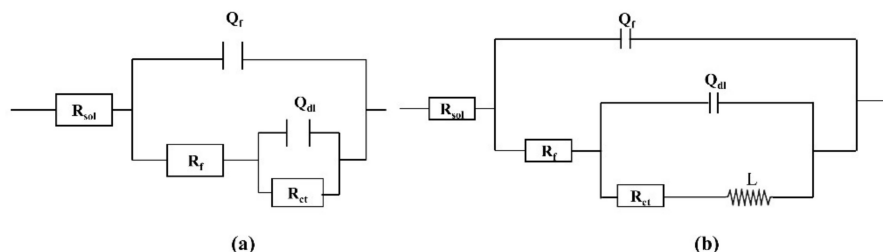


**Figure 7.** Electrochemical equivalent circuits used to fit the measured EIS data in Figure 6. (a) d1–d3; (b) d5–d13.  $R_{\text{sol}}$ : solution resistance;  $Q_f$ : the capacitance of corrosion product film and biofilm;  $R_f$ : resistance of corrosion product film and biofilm;  $Q_{\text{dl}}$ : double-layer capacitance;  $R_{\text{ct}}$ : charge transfer resistance;  $L_{\text{pit}}$ : the inductance in the low-frequency region;  $n$ : dispersion coefficient.

**Table 4.** EIS electrochemical parameter values for the AZ31B magnesium anode during of the 13 days testing time in tidal flat mud with a seawater content 40%.

	$R_{\text{sol}}$ ( $\Omega \text{ cm}^2$ )	$Q_f$ ( $\Omega^{-1} \text{ cm}^{-2} \text{s}^n$ )	$n_f$	$R_f$ ( $\Omega \text{ cm}^2$ )	$Q_{\text{dl}}$ ( $\Omega^{-1} \text{ cm}^{-2} \text{s}^n$ )	$n_{\text{dl}}$	$R_{\text{ct}}$ ( $\Omega \text{ cm}^2$ )	$L_{\text{pit}}$ ( $\text{H} \cdot \text{cm}^2$ )
1 d	47.87	$2.79 \times 10^{-5}$	0.80	2003	$5.71 \times 10^{-4}$	0.80	1559	\
3 d	30.88	$3.74 \times 10^{-5}$	0.88	1469	$2.63 \times 10^{-4}$	0.94	2066	304.4
5 d	27.54	$1.23 \times 10^{-5}$	0.95	37.36	$1.26 \times 10^{-5}$	0.94	1274	1104
7 d	31.88	$2.01 \times 10^{-5}$	0.84	44.92	$1.73 \times 10^{-5}$	0.85	896.2	126.1
9 d	32.98	$1.37 \times 10^{-5}$	0.84	167	$2.61 \times 10^{-5}$	0.82	1637	288.3
11 d	31.06	$5.92 \times 10^{-5}$	0.79	987.1	$5.07 \times 10^{-5}$	0.77	1893	138.7
13 d	22.5	$3.38 \times 10^{-5}$	0.94	15.71	$3.33 \times 10^{-5}$	0.93	1783	161.7

**Table 5.** EIS electrochemical parameter values for the AZ31B magnesium anode during 13 d in tidal flat mud with a seawater content 50%.

	$R_{\text{sol}}$ ( $\Omega \text{ cm}^2$ )	$Q_f$ ( $\Omega^{-1} \text{ cm}^{-2} \text{s}^n$ )	$n_f$	$R_f$ ( $\Omega \text{ cm}^2$ )	$Q_{\text{dl}}$ ( $\Omega^{-1} \text{ cm}^{-2} \text{s}^n$ )	$n_{\text{dl}}$	$R_{\text{ct}}$ ( $\Omega \text{ cm}^2$ )	$L_{\text{pit}}$ ( $\text{H} \cdot \text{cm}^2$ )
1 d	49.37	$2.41 \times 10^{-5}$	0.89	2980	$1.66 \times 10^{-3}$	0.97	1441	\
3 d	52.78	$1.1 \times 10^{-5}$	0.87	41.1	$1.04 \times 10^{-5}$	0.88	902.9	\
5 d	34.68	$1.12 \times 10^{-5}$	0.88	51.54	$1.02 \times 10^{-5}$	0.88	1267	2966
7 d	33.15	$1.03 \times 10^{-5}$	0.95	21.89	$1.92 \times 10^{-5}$	0.94	1023	355.5
9 d	32.58	$1.26 \times 10^{-5}$	0.89	18.6	$2.60 \times 10^{-5}$	0.91	1350	1150
11 d	33.10	$1.59 \times 10^{-5}$	0.91	24.27	$2.33 \times 10^{-5}$	0.92	1470	328.4
13 d	33.97	$1.46 \times 10^{-5}$	0.93	233.8	$2.49 \times 10^{-5}$	0.93	1517	248.5

The change trend of charge transfer resistance values is consistent with the change trend of OCP values (Tables 4–6). By comparing  $R_{\text{ct}}$  values, it can be seen that uniform corrosion occurred in the early stage of the experiment (1–3 d). The charge transfer resistance value had a significant increase and reached the maximum value on the third day. It indicates that the corrosion can be inhibited effectively in the early stage of biofilm formation [43]. This is consistent with the OCP results. During the experimental period between 5 and 13 d, the  $R_{\text{ct}}$  value decreased with the increase in water content. It indicates that the mud with high water content had an increased MIC corrosion rate.

**Table 6.** EIS electrochemical parameter values for the AZ31B magnesium anode during 13 d in tidal flat mud with a seawater content 60%.

	$R_{\text{sol}}$ ( $\Omega \text{ cm}^2$ )	$Q_f$ ( $\Omega^{-1} \text{ cm}^{-2} \text{s}^n$ )	$n_f$	$R_f$ ( $\Omega \text{ cm}^2$ )	$Q_{\text{dl}}$ ( $\Omega^{-1} \text{ cm}^{-2} \text{s}^n$ )	$n_{\text{dl}}$	$R_{\text{ct}}$ ( $\Omega \text{ cm}^2$ )	$L_{\text{pit}}$ ( $\text{H} \cdot \text{cm}^2$ )
1 d	40.17	$2.39 \times 10^{-5}$	0.88	3235	$2.76 \times 10^{-3}$	0.92	1023	\
3 d	57.29	$2.35 \times 10^{-5}$	0.85	4673	$2.17 \times 10^{-3}$	0.88	1559	\
5 d	28.35	$1.43 \times 10^{-5}$	0.87	37.86	$1.41 \times 10^{-5}$	0.91	1228	74.08
7 d	31.87	$1.63 \times 10^{-5}$	0.80	27.2	$1.47 \times 10^{-5}$	0.80	640.6	87.14
9 d	32.68	$1.82 \times 10^{-5}$	0.87	402.7	$1.63 \times 10^{-5}$	0.87	1102	208.2
11 d	36.17	$1.90 \times 10^{-5}$	0.87	37.81	$1.91 \times 10^{-5}$	0.91	1266	219.5
13 d	33.14	$2.07 \times 10^{-5}$	0.87	33.3	$2.04 \times 10^{-5}$	0.90	1206	127.6

Figure 8 shows the potentiodynamic polarization curves of AZ31B magnesium anode samples in tidal flat mud with different water content after 14 d of testing. The sample with increased water content exhibited a reduced corrosion potential value, which is consistent with the change trend of the data obtained by OCP and EIS measurements. The parameters of the Tafel curve analysis are shown in Table 7. Both  $\beta_a$  and  $\beta_c$  were greater than 1, indicating that the corrosion process was controlled by anodic polarization. The corrosion current density (Table 7) increased with the increase in water content, which indicates that the corrosion rate also increased with the increase in the water content.

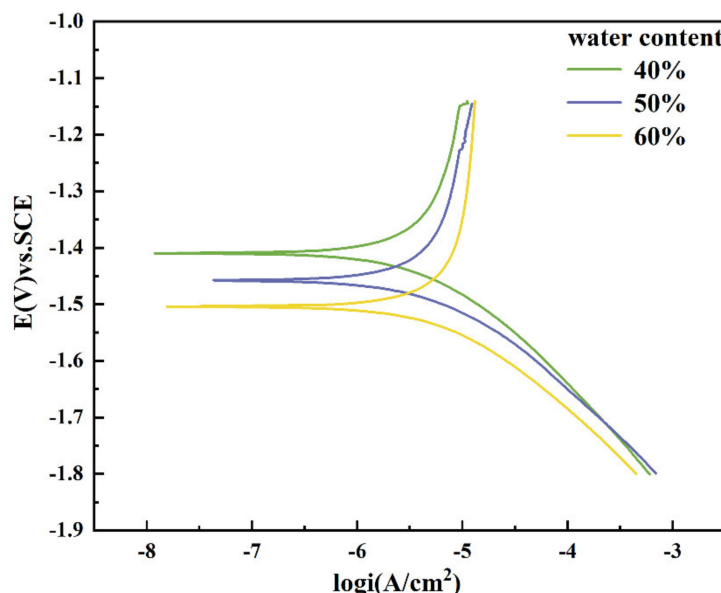


**Figure 8.** Polarization curves of AZ31B magnesium anode coupons after 14 d of testing in the tidal flat mud with seawater contents is 40%, 50% or 60%, respectively.

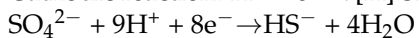
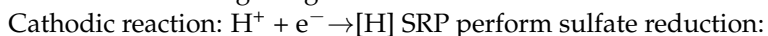
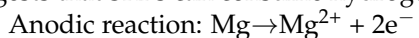
**Table 7.** Electrochemical parameters fitted from Tafel analysis data for coupons after 14 d of testing at varied conditions.  $i_{\text{corr}}$ : corrosion current density;  $E_{\text{corr}}$ : corrosion voltage;  $\beta_a$ : polarization of anodic;  $\beta_c$ : polarization of cathode.

Water Content (%)	$i_{\text{corr}}$ ( $\text{Acm}^{-2}$ )	$E_{\text{corr}}$ (V) vs. SCE	$\beta_a$ (mv/Decade)	$\beta_c$ (mv/Decade)
40	$4.430 \times 10^{-6}$	-1.426	834.2	-139.2
50	$5.670 \times 10^{-6}$	-1.441	711.3	-626.2
60	$9.932 \times 10^{-6}$	-1.511	1077.1	-158.2

#### 4. Discussion

The moisture has a decisive effect on both electrochemical and microbial corrosion in soil environments [44]. Research has shown that a high–water content will decrease

the electrical resistance of the soil [45,46], resulting in high corrosion rates [47]. At the same time, the increase in the water content in the tidal flat mud promotes the growth of SRPs [48]. In the mud environment with low water content, the surface contacting with mud particles has poor permeability, low oxygen content and high oxygen content in contact with the void, resulting in a large number of oxygen concentration cells. With the increase in humidity, oxygen transport to the cathode was blocked, accompanied by the strong proliferation of SRP, as shown in Table 1 in this experiment and the resulting cathode depolarization promotes corrosion [49]. The theory of cathode depolarization [50] suggests that SRPs can consume hydrogen and, thus, promote the corrosion of magnesium:



The consumption of  $\text{H}^+$  in the system promoted the formation of hydrolytic and corrosion products, which led to an acceleration in magnesium corrosion.

We present the conditions, parameters and results of the study of corrosion of different materials by soil water content in Table 8 [29,51–54]:

**Table 8.** The conditions, parameters and results of the study of corrosion of different materials by soil water content.

Experimental Material	Conditions	Parameter	Results
X52 pipeline steel	Diluted $\text{Na}_2\text{SO}_4$ solution+ soil	water content of 5:1, 5:3, 5:5	the MIC rate of the steel is increased by the increasing water content
Cu–9.4Sn and Cu–7.7Sn with 1% of lead	A mixture of the Tunisian soil with distilled water.	Electrolyte soil water content	The increase of the water electrolyte content increases material corrosion rate
carbon steel (SM490A)	A mixture of commercial silica sand (Marutou, Japan) with a particle size of 100 $\mu\text{m}$ and a 3% NaCl aqueous solution	saturation (Sr) = 30%, 50%, 70%, 80%, 90%, 100%	The carbon steel exposed in the saturated soil (Sr = 100%) showed uniform corrosion, non-uniform corrosion in the unsaturated soil (Sr < 100%); the corrosion current density kept constant in the range of 90%Sr to 50%Sr.
High-silicon cast iron	The soil was selected at a depth of 1 m in the grounding.	water content is 15, 20, 25 and 30 per cent	The corrosion rate is the largest when water content is 15% and the corrosion is the lightest when water content is 30%.
Mild steel specimens	Four different types of Libyan soil	soils with different moisture contents (in %): 10, 12.5, 14, 16.5, 20, 25, 30, 50 and 100	Corrosion potentials were found to possess more negative values with rising soil moisture content.

It can be found that different researchers have slightly different results on the relationship between water content and corrosion rate.

This study confirms that a change in the water content in the tidal flat mud environment will aggravate microbial corrosion, thus, accelerating the corrosion of AZ31B magnesium alloy anode material. Data in Figure 2 show that the number of products detected on the surface of samples with 60% water content was significantly higher than the amounts detected on the surface of samples with 40% or 50% water content. Obviously, with 60% water content, the AZ31B magnesium anode was corroded more severely than with less water content. The high numbers of SRPs resulted in an increased thickness of the biofilm containing corrosion products and an increased crystallinity in corrosion products. Combined with the weight-loss data and pitting data in Figures 3 and 4, it is

further demonstrated that increasing water content leads to the number of SRP cells and, thus, accelerates the corrosion rate.

According to the results of the electrochemical data analysis in the early stage of the experiment (1–3 d), the  $R_{ct}$  values of the samples in different water contents showed a trend of increasing first. The SRP biofilms had an inhibitory effect on the corrosion of the samples in the early stage. During days 3 to 7, the  $R_{ct}$  values of samples with different water contents decreased rapidly, which usually corresponded to the logarithmic growth phase of SRPs. At the same time, a loose and porous corrosion product film appeared on the surfaces (Figure 1), which served as cathodic sites. The spots not covered with corrosion products served as anodic sites, where magnesium dissolution took place. Because the cathodic surface area is larger than the total anodic area, local corrosion is more likely to occur [55]. The high-water content in the mud is conducive to the growth of SRP, which, in turn, accelerates the corrosion of the AZ31B magnesium anode and leads to a decrease in the charge transfer resistance. The data from the potentiodynamic polarization curves show that the current density increased with the increase in mud water content (Table 7). The high-water content made the charge transfer of SRPs easier and accelerated the corrosion of AZ31B magnesium anode. Thus, the current density increased. Consequently, the corrosion of the AZ31B magnesium anode became enhanced. The  $i_{corr}$  results of X52 in different water content measured by Liu and Cheng are consistent with the trend observed in the current study [48]: there is the largest  $i_{corr}$  for the specimen tested in the mud with the highest water content (when water content 50%  $i_{corr} = 1.99 \times 10^{-5}$  and when water content 30%  $i_{corr} = 9.65 \times 10^{-7}$ ).

## 5. Conclusions

In this experiment, AZ31B magnesium anode material was taken as this research object. The effect of SRP on the corrosion process of AZ31B magnesium material was investigated at various conditions with different water content of beach muds. The following conclusions can be drawn:

1. SRPs grow well in the tidal flat mud used in this experiment. The increase in the water content in mud is conducive to the growth of SRPs. Thus, the numbers of SRP increase with the increase in moisture;
2. With the increase in the water content and the increase in SRPs, the corrosion process of the AZ31B magnesium anode becomes aggravated;
3. The corrosion rate of the AZ31B magnesium alloy material increases with the increase in the water content of the beach soil. The loose and porous surface morphology of the corrosion products contributes to the occurrence of local corrosion.

**Author Contributions:** Conceptualisation, J.L., J.Z. and X.L.; methodology, R.Z. and B.H.; data curation, J.L.; validation, J.Z. and B.H.; investigation, J.D. and J.Z.; writing—original draft preparation, J.L., X.L. and J.Z.; writing—review and editing, J.Z., W.S. and R.Z.; supervision, J.D., Q.Z. and W.S.; visualization, J.L., Q.Z. and B.H. All authors have read and agreed to the published version of the manuscript.

**Funding:** This research work was financially supported by the National Natural Science Foundation of China (No. 42076043) and the Shandong Provincial Natural Science Foundation (No. ZR2020MD080).

**Data Availability Statement:** The author will provide data upon request.

**Conflicts of Interest:** The authors declare that they have no known competing financial interests or personal relationships that could have appeared to influence the work reported in this paper.

## References

1. Yang, S.; Sun, R.; Chen, K. Self-healing performance and corrosion resistance of phytic acid/cerium composite coating on microarc-oxidized magnesium alloy. *Chem. Eng. J.* **2021**, *428*, 131198. [[CrossRef](#)]
2. Cerreta, E.K.; Fensin, S.J.; Perez-Bergquist, S.J.; Trujillo, C.P.; Morrow, B.M.; Lopez, M.F.; Roach, C.J.; Mathaudhu, S.N.; Anghel, V.; Gray, G.T. The High-Strain-Rate Constitutive Behavior and Shear Response of Pure Magnesium and AZ31B Magnesium Alloy. *Metall. Mater. Trans. A* **2021**, *52*, 3152–3170. [[CrossRef](#)]

3. Chaudry, U.M.; Tekumalla, S.; Gupta, M.; Jun, T.-S.; Hamad, K. Designing highly ductile magnesium alloys: Current status and future challenges. *Crit. Rev. Solid State Mater. Sci.* **2021**, *47*, 194–281. [[CrossRef](#)]
4. Yan, L.; Song, G.-L.; Zheng, D. Magnesium alloy anode as a smart corrosivity detector and intelligent sacrificial anode protector for reinforced concrete. *Corros. Sci.* **2019**, *155*, 13–28. [[CrossRef](#)]
5. Vanaei, H.R.; Eslami, A.; Egbewande, A. A review on pipeline corrosion, in-line inspection (ILI), and corrosion growth rate models. *Int. J. Press. Vessel. Pip.* **2017**, *149*, 43–54. [[CrossRef](#)]
6. Wasim, M.; Shoail, S.; Mubarak, N.M.; Inamuddin; Asiri, A.M. Factors influencing corrosion of metal pipes in soils. *Environ. Chem. Lett.* **2018**, *16*, 861–879. [[CrossRef](#)]
7. Liu, L.; Yuan, K.; Liu, Y.; Pan, S. Microstructure and corrosion behaviour of Al<sub>2</sub>O<sub>3</sub>–13 wt-% TiO<sub>2</sub> laser alloyed magnesium alloys. *Trans. IMF* **2016**, *94*, 99–103. [[CrossRef](#)]
8. Liu, H.; Cao, F.; Song, G.-L.; Zheng, D.; Shi, Z.; Dargusch, M.S.; Atrens, A. Review of the atmospheric corrosion of magnesium alloys. *J. Mater. Sci. Technol.* **2019**, *35*, 2003–2016. [[CrossRef](#)]
9. Wu, W.; Zhang, F.; Li, Y.; Song, L.; Jiang, D.; Zeng, R.-C.; Tjong, S.C.; Chen, D.-C. Corrosion resistance of dodecanethiol-modified magnesium hydroxide coating on AZ31 magnesium alloy. *Appl. Phys. A* **2019**, *126*, 8. [[CrossRef](#)]
10. Xu, L.; Liu, X.; Sun, K.; Fu, R.; Wang, G. Corrosion Behavior in Magnesium-Based Alloys for Biomedical Applications. *Materials* **2022**, *15*, 2613. [[CrossRef](#)]
11. Yan, T.; Tan, L.; Zhang, B.; Yang, K. Fluoride Conversion Coating on Biodegradable AZ31B Magnesium Alloy. *J. Mater. Sci. Technol.* **2014**, *30*, 666–674. [[CrossRef](#)]
12. Yan, D.; Wang, Y.; Liu, J.; Song, D.; Zhang, T.; Liu, J.; He, F.; Zhang, M.; Wang, J. Self-healing system adapted to different pH environments for active corrosion protection of magnesium alloy. *J. Alloys Compd.* **2020**, *824*, 153918. [[CrossRef](#)]
13. Meng, Y.; Gao, H.; Hu, J.; Gao, L. Effect of pH value on the corrosion and corrosion fatigue behavior of AM60 magnesium alloy. *J. Mater. Res.* **2019**, *34*, 1054–1063. [[CrossRef](#)]
14. Simanjuntak, S.; Cavanaugh, M.; Gandel, D.; Easton, M.; Gibson, M.; Birbilis, N. The Influence of Iron, Manganese, and Zirconium on the Corrosion of Magnesium: An Artificial Neural Network Approach. *Corrosion* **2015**, *71*, 199–208. [[CrossRef](#)]
15. Pan, H.; Wang, L.; Lin, Y.; Ge, F.; Zhao, K.; Wang, X.; Cui, Z. Mechanistic study of ammonium-induced corrosion of AZ31 magnesium alloy in sulfate solution. *J. Mater. Sci. Technol.* **2020**, *54*, 1–13. [[CrossRef](#)]
16. Li, Z.; Shang, Z.; Wei, X.; Zhao, Q. Corrosion resistance and cytotoxicity of AZ31 magnesium alloy with N<sup>+</sup> ion implantation. *Mater. Technol.* **2019**, *34*, 730–736. [[CrossRef](#)]
17. Khouzani, M.K.; Bahrami, A.; Hosseini-Abhari, A.; Khandouzi, M.; Taheri, P. Microbiologically Influenced Corrosion of a Pipeline in a Petrochemical Plant. *Metals* **2019**, *9*, 459. [[CrossRef](#)]
18. Li, S.; Li, L.; Qu, Q.; Kang, Y.; Zhu, B.; Yu, D.; Huang, R. Extracellular electron transfer of *Bacillus cereus* biofilm and its effect on the corrosion behaviour of 316L stainless steel. *Colloids Surf. B Biointerfaces* **2018**, *173*, 139–147. [[CrossRef](#)]
19. Spark, A.; Wang, K.; Cole, I.; Law, D.; Ward, L. Microbiologically influenced corrosion: A review of the studies conducted on buried pipelines. *Corros. Rev.* **2020**, *38*, 231–262. [[CrossRef](#)]
20. Liu, H.; Cheng, Y.F. Microbial corrosion of initial perforation on abandoned pipelines in wet soil containing sulfate-reducing bacteria. *Colloids Surf. B Biointerfaces* **2020**, *190*, 110899. [[CrossRef](#)]
21. Chen, S.; Wang, P.; Zhang, D. Corrosion behavior of copper under biofilm of sulfate-reducing bacteria. *Corros. Sci.* **2014**, *87*, 407–415. [[CrossRef](#)]
22. Gu, T.; Jia, R.; Unsal, T.; Xu, D. Toward a better understanding of microbiologically influenced corrosion caused by sulfate reducing bacteria. *J. Mater. Sci. Technol.* **2018**, *35*, 631–636. [[CrossRef](#)]
23. Xu, L.; Guan, F.; Ma, Y.; Zhang, R.; Zhang, Y.; Zhai, X.; Dong, X.; Wang, Y.; Duan, J.; Hou, B. Inadequate dosing of THPS treatment increases microbially influenced corrosion of pipeline steel by inducing biofilm growth of *Desulfovibrio hontrensis* SY-21. *Bioelectrochemistry* **2022**, *145*, 108048. [[CrossRef](#)] [[PubMed](#)]
24. Li, X.; Duan, J.; Xiao, H.; Li, Y.; Liu, H.; Guan, F.; Zhai, X. Analysis of Bacterial Community Composition of Corroded Steel Immersed in Sanya and Xiamen Seawaters in China via Method of Illumina MiSeq Sequencing. *Front. Microbiol.* **2017**, *8*, 1737. [[CrossRef](#)]
25. Lin, R.; Liu, C. Surface anticorrosion methods and prospects of AZ91 series magnesium alloys. *Cast. Tech.* **2011**, *32*, 566–568.
26. Liu, F.; Zhang, J.; Zhang, S.; Li, W.; Duan, J.; Hou, B. Effect of sulphate reducing bacteria on corrosion of Al-Zn-In-Sn sacrificial anodes in marine sediment. *Mater. Corros.* **2010**, *63*, 431–437. [[CrossRef](#)]
27. Liu, F.; Zhang, J.; Sun, C.; Yu, Z.; Hou, B. The corrosion of two aluminium sacrificial anode alloys in SRB-containing sea mud. *Corros. Sci.* **2014**, *83*, 375–381. [[CrossRef](#)]
28. Elumalai, P.; Parthipan, P.; Narenkumar, J.; Sarankumar, R.K.; Karthikeyan, O.P.; Rajasekar, A. Influence of Thermophilic Bacteria on Corrosion of Carbon Steel in Hyper Chloride Environment. *Int. J. Environ. Res.* **2017**, *11*, 339–347. [[CrossRef](#)]
29. Lan, X.; Zhang, J.; Wang, Z.; Zhang, R.; Sand, W.; Zhang, L.; Duan, J.; Zhu, Q.; Hou, B. Corrosion of an AZ31B Magnesium Alloy by Sulfate-Reducing Prokaryotes in a Mudflat Environment. *Microorganisms* **2022**, *10*, 839. [[CrossRef](#)]
30. Cui, L.; Liu, Z.; Hu, P.; Shao, J. Laboratory Investigation of Microbiologically Influenced Corrosion of X80 Pipeline Steel by Sulfate-Reducing Bacteria. *J. Mater. Eng. Perform.* **2021**, *30*, 7584–7596. [[CrossRef](#)]
31. Wu, J.; Zhang, D.; Wang, P.; Cheng, Y.; Sun, S.; Sun, Y.; Chen, S. The influence of *Desulfovibrio* sp. and *Pseudoalteromonas* sp. on the corrosion of Q235 carbon steel in natural seawater. *Corros. Sci.* **2016**, *112*, 552–562. [[CrossRef](#)]

32. Fu, Q.; Xu, J.; Wei, B.; Qin, Q.; Bai, Y.; Yu, C.; Sun, C. Biologically competitive effect of *Desulfovibrio desulfurican* and *Pseudomonas stutzeri* on corrosion of X80 pipeline steel in the Shenyang soil solution. *Bioelectrochemistry* **2022**, *145*, 108051. [[CrossRef](#)] [[PubMed](#)]
33. Yang, P.; Bu, Z.; An, Y.; Zhou, H.; Li, Y.; Chen, J. Hot corrosion product and corrosion layer evolution of  $\text{La}_2(\text{Zr}_{0.75}\text{Ce}_{0.25})_2\text{O}_7$  coating exposed to vanadate-sulfate salts at 1050 °C. *Ceram. Int.* **2022**, *48*, 13014–13023. [[CrossRef](#)]
34. Al Abbas, F.M.; Williamson, C.; Bhola, S.M.; Spear, J.R.; Olson, D.L.; Mishra, B.; Kakpovbia, A.E. Influence of sulfate reducing bacterial biofilm on corrosion behavior of low-alloy, high-strength steel (API-5L X80). *Int. Biodeterior. Biodegrad.* **2013**, *78*, 34–42. [[CrossRef](#)]
35. Fan, Y.; Chen, C.; Zhang, Y.; Liu, H. Early corrosion behavior of X80 pipeline steel in a simulated soil solution containing *Desulfovibrio desulfuricans*. *Bioelectrochemistry* **2021**, *141*, 107880. [[CrossRef](#)]
36. Shahryari, Z.; Gheisari, K.; Motamed, H. Effect of sulfate reducing *Citrobacter* sp. strain on the corrosion behavior of API X70 microalloyed pipeline steel. *Mater. Chem. Phys.* **2019**, *236*, 121799. [[CrossRef](#)]
37. Guan, F.; Duan, J.; Zhai, X.; Wang, N.; Zhang, J.; Lu, D.; Hou, B. Interaction between sulfate-reducing bacteria and aluminum alloys—Corrosion mechanisms of 5052 and Al-Zn-In-Cd aluminum alloys. *J. Mater. Sci. Technol.* **2020**, *36*, 55–64. [[CrossRef](#)]
38. Dou, W.; Liu, J.; Cai, W.; Wang, D.; Jia, R.; Chen, S.; Gu, T. Electrochemical investigation of increased carbon steel corrosion via extracellular electron transfer by a sulfate reducing bacterium under carbon source starvation. *Corros. Sci.* **2019**, *150*, 258–267. [[CrossRef](#)]
39. Trif, L.; Shaban, A.; Telegli, J. Electrochemical and surface analytical techniques applied to microbiologically influenced corrosion investigation. *Corros. Rev.* **2018**, *36*, 349–363. [[CrossRef](#)]
40. Moradi, M.; Ghiara, G.; Spotorno, R.; Xu, D.; Cristiani, P. Understanding biofilm impact on electrochemical impedance spectroscopy analyses in microbial corrosion and microbial corrosion inhibition phenomena. *Electrochim. Acta* **2022**, *426*, 140803. [[CrossRef](#)]
41. Yin, L.; Xu, D.; Yang, C.; Xi, T.; Chen, X.; Yang, K. Ce addition enhances the microbially induced corrosion resistance of Cu-bearing 2205 duplex stainless steel in presence of sulfate reducing bacteria. *Corros. Sci.* **2020**, *179*, 109141. [[CrossRef](#)]
42. Unsal, T.; Ilhan-Sungur, E.; Arkan, S.; Cansever, N. Effects of Ag and Cu ions on the microbial corrosion of 316L stainless steel in the presence of *Desulfovibrio* sp. *Bioelectrochemistry* **2016**, *110*, 91–99. [[CrossRef](#)] [[PubMed](#)]
43. Bao, Q.; Zhang, D.; Lv, D.; Wang, P. Effects of two main metabolites of sulphate-reducing bacteria on the corrosion of Q235 steels in 3.5wt.% NaCl media. *Corros. Sci.* **2012**, *65*, 405–413. [[CrossRef](#)]
44. Sani, F.M. Evaluation of the Simultaneous Effects of Sulfate Reducing Bacteria, Soil Type and Moisture Content on Corrosion Behavior of Buried Carbon Steel API 5L X65. *Int. J. Electrochem. Sci.* **2016**, *11*, 3887–3907. [[CrossRef](#)]
45. Akkouche, R.; Rémazeilles, C.; Jeannin, M.; Barbalat, M.; Sabot, R.; Refait, P. Influence of soil moisture on the corrosion processes of carbon steel in artificial soil: Active area and differential aeration cells. *Electrochim. Acta* **2016**, *213*, 698–708. [[CrossRef](#)]
46. Quej-Ake, L.; Marín-Cruz, J.; Contreras, A. Electrochemical study of the corrosion rate of API steels in clay soils. *Anti Corros. Methods Mater.* **2017**, *64*, 61–68. [[CrossRef](#)]
47. Sun, B.; Liao, W.; Li, Z.; Liu, Z.; Du, C. Corrosion behavior of X65 pipeline steel in coastal areas. *Anti Corros. Methods Mater.* **2019**, *66*, 286–293. [[CrossRef](#)]
48. Liu, H.; Cheng, Y.F. Mechanism of microbiologically influenced corrosion of X52 pipeline steel in a wet soil containing sulfate-reduced bacteria. *Electrochim. Acta* **2017**, *253*, 368–378. [[CrossRef](#)]
49. Wei, B.; Xu, J.; Fu, Q.; Qin, Q.; Bai, Y.; Sun, C.; Wang, C.; Wang, Z.; Ke, W. Effect of sulfate-reducing bacteria on corrosion of X80 pipeline steel under disbonded coating in a red soil solution. *J. Mater. Sci. Technol.* **2021**, *87*, 1–17. [[CrossRef](#)]
50. Cordruwisch, R.; Widdel, F. Corroding Iron as a hydrogen source for sulfate reduction in growing cultures of sulfate-reducing bacteria. *Appl. Microbiol. Biotechnol.* **1986**, *25*, 169–174. [[CrossRef](#)]
51. Souissi, N.; Triki, E. Early stages of copper corrosion behaviour in a Tunisian soil. *Mater. Corros.* **2009**, *61*, 695–701. [[CrossRef](#)]
52. Hirata, R.; Ooi, A.; Tada, E.; Nishikata, A. Influence of the degree of saturation on carbon steel corrosion in soil. *Corros. Sci.* **2021**, *189*, 109568. [[CrossRef](#)]
53. Ding, D.; Zhang, Y.; Yu, X.; Fang, B.; Guo, J.; Li, J.; Liu, L.; Du, C. Effects of environmental factors on corrosion behavior of high-silicon cast iron in Shanxi soil medium. *Anti Corros. Methods Mater.* **2018**, *65*, 538–546. [[CrossRef](#)]
54. Ezuber, H.M.; Alshater, A.; Hossain, S.M.Z.; El-Basir, A. Impact of Soil Characteristics and Moisture Content on the Corrosion of Underground Steel Pipelines. *Arab. J. Sci. Eng.* **2020**, *46*, 6177–6188. [[CrossRef](#)]
55. Liu, H.; Cheng, Y.F. Microbial corrosion of X52 pipeline steel under soil with varied thicknesses soaked with a simulated soil solution containing sulfate-reducing bacteria and the associated galvanic coupling effect. *Electrochim. Acta* **2018**, *266*, 312–325. [[CrossRef](#)]